ATLAS NOTE

ATLAS-CONF-2013-056

June 20, 2013

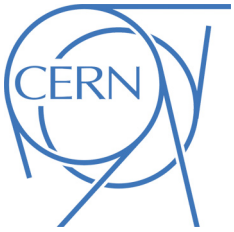

Search for pair production of new heavy quarks that decay to a Z boson and a third generation quark in pp collisions at $\sqrt{s} = 8$ TeV with the ATLAS detector

The ATLAS Collaboration

Abstract

A search is presented for the production of a new heavy quark with its antiparticle, assuming the new quark has a significant branching ratio to decay into a Z boson and a third generation Standard Model quark. In the case of a new charge $+2/3$ quark (T) the decay targeted is $T \to Zt$, while for a new charge $-1/3$ quark (B) the decay targeted is $B \to Zb$. The search uses a dataset corresponding to 14.3 fb^{-1} of pp collisions at $\sqrt{s} = 8$ TeV recorded in 2012 with the ATLAS detector at the CERN Large Hadron Collider. Selected events contain a high transverse momentum Z boson candidate reconstructed from a pair of oppositely charged electrons or muons. Additionally, the presence of at least two jets possessing properties consistent with the decay of a b hadron is required, as well as large total transverse momentum of all central jets in the event. No significant excess of events above the Standard Model expectation is observed, and upper limits are derived for vector-like quarks of various masses in a two-dimensional plane of branching ratios. Under branching ratio assumptions corresponding to a weak-isospin singlet scenario, a T (B) quark with mass lower than 585 (645) GeV is excluded at the 95% confidence level. Under branching ratio assumptions corresponding to a particular weak-isospin doublet scenario, a T (B) quark with mass lower than 680 (725) GeV is excluded at the 95% confidence level.

ATLAS-CONF-2013-056
25 June 2013

1 Introduction

A cornerstone of the Standard Model (SM) is the formulation of the electroweak interactions as arising from a spontaneously broken gauge symmetry. Experiments over the past four decades have confirmed this hypothesis with precision, in particular the results of the CERN LEP collider program [1, 2]. However, the nature of the symmetry breaking mechanism is not yet determined. Recently, the ATLAS and CMS collaborations have reported observations [3, 4] of a new particle produced at the CERN Large Hadron Collider (LHC) with properties thus far consistent with those predicted of the SM Higgs boson. The default electroweak symmetry breaking mechanism, whereby a weak-isospin doublet of fundamental scalar fields obtains a vacuum expectation value, therefore remains a valid hypothesis.

Even with the existence of a Higgs-like particle confirmed, the SM cannot be considered a complete description of Nature. For example, the theory does not predict the fermion generations and mass hierarchy, the origin of the matter-antimatter asymmetry in the universe, nor does it possess a viable dark matter particle or describe gravitational interactions. Thus, the SM is generally regarded as a low energy approximation of a more fundamental theory with new degrees of freedom and symmetries that manifest themselves at higher energy. In fact, the SM violates a concept of naturalness [5] when extrapolated to energies above the electroweak scale, as fine tuning is required to compensate the quadratic mass divergences of fundamental scalar fields.

One candidate for such a theory is supersymmetry (SUSY) [6]. The new degrees of freedom in this case are the SUSY partners of the SM particles. The existence of SUSY partners could ameliorate the naturalness problem, generating new terms that cancel the quadratically divergent ones. Despite the appeal of low scale SUSY in this and several others respects, results of direct searches for SUSY partners have thus far yielded null results [7].

An alternative class of models are those in which the electroweak symmetry is broken dynamically by a new strong interaction [8], such as in Topcolor [9], Little Higgs [10, 11], and Composite Higgs [12] scenarios. A recurring feature in these models is the appearance of vector-like quarks, defined as quarks for which both chiralities have the same transformation properties under the electroweak gauge group. These quarks may not be fundamental, but possibly composite states associated with the strongly coupled sector, and would mix with like-charge SM quarks [13]. In the case of the top quark, such a vector-like quark is referred to as a *top-partner*, and the interplay between the two may play a critical role in regulating the Higgs mass divergences. Hence, vector-like quarks emerge as a characteristic feature of several non-SUSY *natural models* [14].

Search strategies for vector-like quarks have been described previously [15, 16, 17, 18]. Results of searches for chiral fourth-generation quarks apply, though the interpretation of exclusion limits was difficult in the past when the quarks were assumed to decay entirely via the charged-current mode. The GIM mechanism [19] does not apply to vector-like quarks, and hence tree-level neutral-current decays are possible [20]. Recently, searches traditionally targeting chiral quarks, and hence the charged-current decay mode, have provided vector-like quark interpretations as well [21, 22]. A few dedicated searches in the neutral-current channels have also been carried out [23, 24], most recently in a $T \to Ht$ targeted search [25].

This note describes an ATLAS search with 8 TeV data for pair production of charge $+2/3$ (T) or $-1/3$ (B) vector-like quarks assuming a significant branching fraction for the neutral-current decay to a Z boson and a third generation quark ($T \to Zt$ or $B \to Zb$). Events are selected that contain a high transverse momentum Z boson candidate reconstructed with oppositely charged leptons, at least two b-tagged jets, and large total transverse momentum of the central jets in the event. After the final event selection, the invariant mass of the Z boson candidate and the b-tagged jet with the highest transverse momentum, $m(Zb)$, is tested for a signal-like excess of events beyond the Standard Model prediction.

2 The ATLAS Detector

The ATLAS detector [26] identifies and measures the momentum and energy of particles created in proton-proton (pp) collisions at the LHC. It has a cylindrical geometry, approximate 4π solid angle coverage, and consists of particle-tracking detectors, electromagnetic and hadronic calorimeters, and a muon spectrometer. At small radii transverse to the beamline, the inner tracking system utilizes fine-granularity pixel and microstrip detectors designed to provide precision track impact parameter and secondary vertex measurements. These silicon-based detectors cover the pseudorapidity range $|\eta| < 2.5$ [1]. A gas-filled straw tube tracker complements the silicon tracker at larger radii. The tracking detectors are immersed in a 2 T magnetic field produced by a thin superconducting solenoid located in the same cryostat as the barrel electromagnetic (EM) calorimeter. The EM calorimeters employ lead absorbers and utilize liquid argon as the active medium. The barrel EM calorimeter covers $|\eta| < 1.5$, and the end-cap EM calorimeters $1.4 < |\eta| < 3.2$. Hadronic calorimetry in the region $|\eta| < 1.7$ is achieved using steel absorbers and scintillating tiles as the active medium. Liquid argon calorimetry with copper absorbers is employed in the hadronic end-cap calorimeters, which cover the region $1.5 < |\eta| < 3.2$. The muon spectrometer measures the deflection of muon tracks within $|\eta| < 2.7$ using multiple layers of high-precision tracking chambers located in a toroidal field of approximately 0.5 T and 1 T in the central and end-cap regions of ATLAS, respectively. The muon spectrometer is also instrumented with separate trigger chambers covering $|\eta| < 2.4$. A three-level trigger is used by the ATLAS detector. The first-level trigger is implemented in custom electronics, using a subset of detector information to reduce the event rate to a design value of 75 kHz. The second and third levels use software algorithms running on PC farms to yield a recorded event rate of about 300 Hz.

3 Reconstructed Physics Objects

The primary physics objects considered in this search are electrons, muons, jets, and b-tagged jets. A summary of the reconstruction methods and identification criteria applied to each is given below.

Electron candidates [27] are reconstructed from energy deposits (clusters) in the EM calorimeter that are matched to corresponding reconstructed tracks in the inner detector. The candidates are required to have a transverse energy, E_{T}, greater than 25 GeV and $|\eta_{\mathrm{cluster}}| < 2.47$ (where $|\eta_{\mathrm{cluster}}|$ is the pseudorapidity of the calorimeter cluster associated with the electron candidate). Candidates in the transition region between barrel and end-cap calorimeters, $1.37 < |\eta_{\mathrm{cluster}}| < 1.52$, are excluded. Electron candidates in this analysis satisfy medium quality requirements on the EM cluster and associated track. Additionally, the longitudinal impact parameter of the electron track with respect to the selected primary vertex (see Sec. 4) is required to be less than 2 mm. No requirements on calorimeter energy or track isolation are made beyond the track isolation requirement that may be applied in the electron trigger selection.

Muon candidates are reconstructed from track segments in the various layers of the muon spectrometer and matched to corresponding reconstructed tracks in the inner detector. The final candidates are refitted using the complete track information from both detector systems. A muon candidate is required to have a transverse momentum, p_{T}, greater than 25 GeV and $|\eta| < 2.5$. The hit pattern in the inner detector must be consistent with a well reconstructed track, and the longitudinal impact parameter of the muon track with respect to the selected primary vertex of the event is required to be less than 2 mm. Muons are also required to satisfy a $p_{\mathrm{T}}-$dependent track-based isolation requirement: the scalar sum of the track p_{T} in a $\Delta R \equiv \sqrt{\Delta\eta^2 + \Delta\phi^2}$ cone of variable radius $\Delta R < 10\ \mathrm{GeV}/p_{\mathrm{T}}^{\mu}$ around the muon

[1] ATLAS uses a right-handed coordinate system with its origin at the nominal interaction point (IP) in the centre of the detector and the z-axis coinciding with the axis of the beam pipe. The x-axis points from the IP to the centre of the LHC ring, and the y-axis points upward. Cylindrical coordinates (r,ϕ) are used in the transverse plane, ϕ being the azimuthal angle around the beam pipe. The pseudorapidity is defined in terms of the polar angle θ as $\eta = -\ln\tan(\theta/2)$.

(excluding the muon itself) must be less than 5% of the muon transverse momentum, p_{T}^{μ}.

Jets are reconstructed with the anti-k_t algorithm [28, 29, 30] with a radius parameter $R = 0.4$ from calibrated topological clusters built from energy deposits in the calorimeters. Prior to jet finding, a local cluster calibration scheme [31] is applied to correct the topological cluster energies for the effects of non-compensation, dead material, and out-of-cluster leakage. The corrections are obtained from simulation of charged and neutral particles. After energy calibration [32] jets are required to satisfy $p_{\mathrm{T}} > 25$ GeV and $|\eta| < 2.5$. Selected jets separated by $\Delta R < 0.2$ from an electron candidate are removed to avoid counting electrons as jets. Subsequently, electron and muon candidates within $\Delta R = 0.4$ of the axis of a selected jet are removed to avoid selecting leptons candidates from hadron decays.

To reduce selected jets that originate from secondary pp interactions, a requirement on a variable referred to as the "jet vertex fraction" (JVF) is made. The requirement ensures that at least 50% of the sum of the p_{T} of tracks with $p_{\mathrm{T}} > 0.5$ GeV associated with a jet comes from tracks compatible with originating from the primary vertex.

Jets are identified as originating from the hadronization of a b quark (b-tagging) via an algorithm [33] using multivariate techniques to combine information from the impact parameters of displaced tracks as well as topological properties of secondary and tertiary decay vertices reconstructed within the jet. The working point used corresponds to a 70% efficiency to tag a b-quark, with a light-jet rejection factor of ~ 130 and a charm jet rejection factor of 5, as determined for b-tagged jets with $p_{\mathrm{T}} > 20$ GeV and $|\eta| < 2.5$ in simulated $t\bar{t}$ events.

4 Data Sample and Event Preselection

The data analyzed in this search were collected with the ATLAS detector between April and October 2012 during LHC pp collisions at $\sqrt{s} = 8$ TeV and correspond to an integrated luminosity of 14.3 ± 0.5 fb^{-1} [34]. Events recorded by single electron or muon triggers under stable beam conditions and for which all detector subsystems were operational are considered. Single lepton triggers with different p_{T} thresholds are combined to increase the overall efficiency. The p_{T} thresholds are 24 and 60 GeV for electron-triggers and 24 and 36 GeV for muon-triggers. The lower threshold triggers include isolation requirements on the candidate leptons, resulting in inefficiencies at higher p_{T} that are recovered by the higher p_{T} threshold triggers. The trigger isolation criteria are looser or identical than the requirements placed on the final reconstructed electrons and muons.

Events satisfying the trigger requirements must also have a reconstructed vertex with at least five associated tracks, consistent with the beam collision region in the $x-y$ plane. If more than one such vertex is found, the primary vertex selected is the one with the largest sum of the squared transverse momenta of its associated tracks. Events selected for analysis contain at least one pair of same flavor reconstructed leptons (electrons or muons) with opposite electric charge, and at least one reconstructed lepton in the event must match ($\Delta R < 0.15$) a lepton reconstructed by the high-level trigger. Reconstructed Z boson candidates are formed if the invariant mass of same flavor and opposite charge lepton pairs differs from the Z boson mass by less than 15 GeV. If more than one Z boson candidate is reconstructed in an event, the one whose mass is closest to the Z boson mass is considered.

5 Signal Modeling

At the LHC, new quarks with masses below $O(1\ \mathrm{TeV})$ would be predominantly produced in pairs via the strong interaction, as illustrated in Fig. 1(a). At higher masses, single production mediated by the electroweak interactions could potentially dominate, depending on the strength of the interaction between the new quarks and the weak gauge bosons. This search considers pair production exclusively, and the

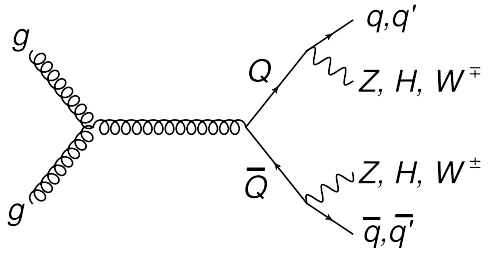

(a)

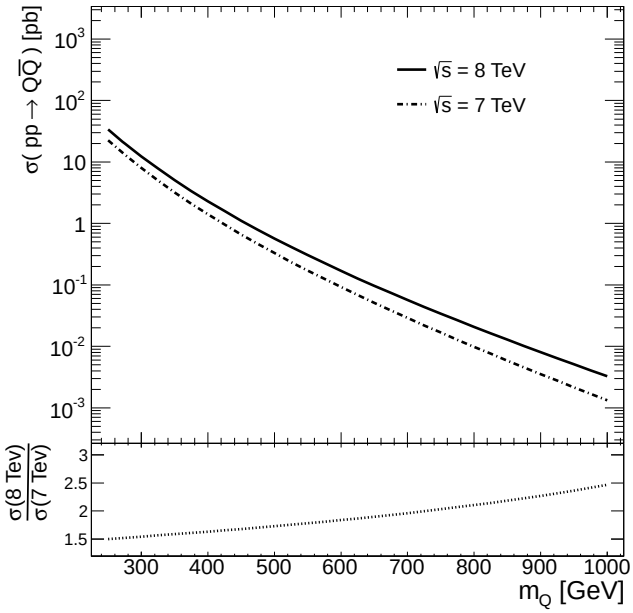

(b)

Figure 1: A representative diagram (a) illustrating heavy quark pair production and vector-like decay modes. The pair production cross section versus quark mass (b) as predicted by HATHOR [35] for pp collisions at $\sqrt{s} = 7$ TeV and 8 TeV. The bottom panel shows the 8 TeV/7 TeV cross section ratio.

cross section is shown in Fig. 1(b) as a function of the new quark mass. The prediction has been computed with HATHOR v1.2 [35], an approximate next-to-next-to-leading-order (NNLO) calculation, using the MSTW2008 NNLO 90% C.L. [36] set of parton distribution functions (PDFs), and is independent of the electroweak quantum numbers of the new quark. The 8 TeV cross section ranges from approximately 5 pb for a quark mass of 350 GeV to approximately 10 fb for a quark mass of 850 GeV. Uncertainties have been calculated according to the MSTW prescription [37] and range from approximately 10 to 20% in the mass range considered in this analysis.

Once produced, the final state topology depends on the decay modes of the new quarks. Unlike chiral quarks, where only the charged-current decay mode occurs at tree-level due to GIM suppression of the neutral-current modes, vector-like quark decays can proceed at tree-level to a W, Z, or H boson plus a SM quark. Additionally, vector-like quarks are generally assumed to couple preferentially to third generation SM quarks, as the mixing is proportional to the mass of the SM quark [38]. Therefore, Fig. 1(a) depicts a T or a B vector-like quark, represented by Q, decaying to either a SM t or b quark, represented by q/q', and a Z, H, or W boson. The branching ratios of a T quark versus its mass, as computed by PROTOS v2.2 [39, 16], are shown in Fig. 2(a). A weak-isospin singlet T quark hypothesis is depicted, as well as a T that is part of a weak-isospin doublet. The doublet prediction is valid for an (X,T) doublet, where the charge of the X quark is $+5/3$, as well as a (T,B) doublet when a mixing assumption of $V_{Tb} \ll V_{tB}$ is made [16]. Note that $BR(T \to Wb) = 0$ in the doublet cases. Similarly, Fig. 2(b) shows the branching ratio of a B quark versus mass for the singlet and doublet hypotheses. In the case of a (T,B) doublet, $BR(B \to Wt) = 1$. Branching ratio values are also shown for a (B,Y) doublet, where the charge of the Y quark is $-4/3$. The charged-current mode, $BR(B \to Wt)$, is absent in this case.

Simulated samples of leading-order pair production events were generated for the $T\bar{T}$ and $B\bar{B}$ hypotheses with PROTOS v2.2 interfaced with PYTHIA [40] v6.421 for parton shower and fragmentation, and using the MSTW 2008 LO 68% C.L. [36] set of PDFs. The cross section normalization of these

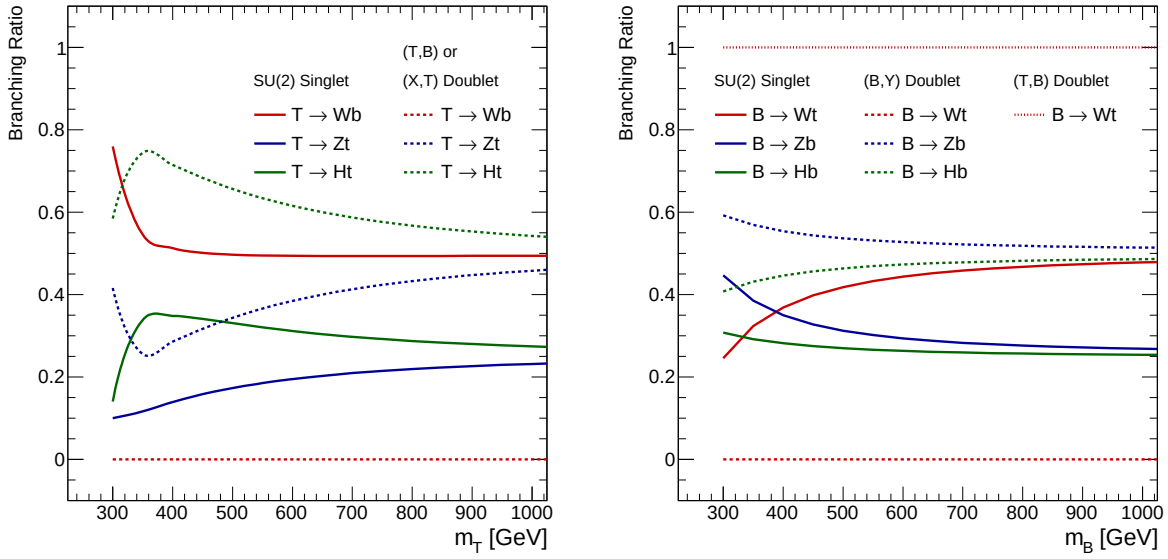

(a) (b)

Figure 2: Vector-like T quark branching ratios (a) to the Wb, Zt, and Ht decay modes versus mass, computed with PROTOS [39] for an $SU(2)$ singlet and two types of doublets. Likewise, vector-like B quark branching ratios (b) to the Wt, Zb, and Hb decay modes for a singlet and two types of doublets. The X quark in an (X,T) doublet has charge $+5/3$, and the Y quark in a (B,Y) doublet has charge $-4/3$.

samples is set by the HATHOR prediction. The vector-like quarks were decayed in the charged- (W) and neutral-current (Z,H) modes assuming a $1/3$ branching ratio for each. Arbitrary sets of branching ratios consistent with the three modes summing to unity are obtained by reweighting the samples using particle-level information. A SM Higgs boson with a mass of 125 GeV is assumed. The primary set of samples span quark masses between 350 GeV and 850 GeV in steps of 50 GeV and were produced assuming $SU(2)$ singlet couplings. Additional samples were produced at two mass points (350 and 600 GeV) using $SU(2)$ doublet couplings in order to confirm that the kinematic differences between singlet and doublet couplings are negligible in this analysis. The above samples were passed through a fast detector simulation [41], while additional samples with quark masses of 400, 600 and 800 GeV were also produced using full detector simulation [42] for validation. All signal samples were filtered at the generator level to require the presence of at least one electron or muon with $p_{\mathrm{T}} > 10$ GeV and $|\eta| < 2.8$.

6 Background Modeling

The SM backgrounds in this analysis are predicted primarily with simulated samples normalized to next-to-leading order or higher cross section calculations. Unless stated otherwise, all samples for SM processes are passed through a full detector simulation. Two leading-order multi-parton event generators, ALPGEN [43] and SHERPA [44], were compared at each stage of the analysis to provide a robust characterization of the dominant Z+jets background. The cross section normalization of both is set by the NNLO prediction calculated with the DYNNLO program [45]. In this note, the SHERPA predictions are shown throughout, as the statistical uncertainties when using these samples are significantly smaller than those associated with the ALPGEN samples, particularly in the final stages of the event selection.

The ALPGEN Z+jets samples were produced using v2.13 with the CTEQ6L1 [46] PDF set and interfaced to PYTHIA [40] v6.421 for parton-shower and hadronization. Separate inclusive Z+jets and dedicated $Z + c\bar{c}$+jets and $Z + b\bar{b}$+jets samples were simulated. Heavy flavor quarks in the former arise

from the parton shower, while in the latter they can be produced directly in the matrix element. To avoid double-counting of partonic configurations generated both by the matrix element and the parton shower, a parton-jet matching scheme [47] is employed in the generation of the samples. Likewise, to remove double-counting when combining the inclusive and dedicated heavy flavor samples, another algorithm is employed based on the angular separation between the heavy quarks ($Q = b, c$). The matrix-element prediction is used if $\Delta R(Q, \bar{Q}) > 0.4$, and the parton-shower prediction is used otherwise.

The SHERPA Z+jets samples were produced using v1.4.1 with the CT10 [48] PDF set, and generated setting the charm and bottom quarks to be massive. Filters are used to divide the samples into events containing a bottom hadron, events without a bottom hadron but containing a charm hadron, and events with neither a charm nor a bottom hadron. In this note, the Z+bottom background category corresponds to the bottom hadron filtered samples, while the Z+light category combines those without a bottom hadron. To increase the statistical precision of the prediction of events with large Z boson transverse momentum, $p_{\mathrm{T}}(Z)$, each hadron filtered sample is produced in different $p_{\mathrm{T}}(Z)$ intervals: inclusive, $70-140$ GeV, $140-280$ GeV, $280-500$ GeV, and >500 GeV. Samples in the first three ranges are reconstructed with a fast detector simulation while the latter two use full detector simulation.

After SM Z+jets processes, the pair production of top quarks ($t\bar{t}$) is the next most significant background source at the final stages of event selection. The $t\bar{t}$ cross section is determined by the HATHOR prediction, computed as in the signal hypothesis, but setting the top quark mass to be 172.5 GeV. Simulated $t\bar{t}$ events are produced using POWHEG [49] for the matrix element with the CT10 PDF set. Parton shower and hadronization are performed with PYTHIA.

Other small SM background processes modeled with simulation are diboson, single top, $t\bar{t}+W/Z$, and W+jets processes. The diboson processes (WW, WZ, and ZZ) are simulated with ALPGEN interfaced to HERWIG [50] for parton shower and hadronization, and normalized to NLO cross section predictions [51]. Samples generated with MC@NLO [52] interfaced to HERWIG are used to estimate the Wt and s-channel single top processes, while ACERMC [53] interfaced to PYTHIA is used to estimate the t-channel process. The single top processes are normalized to NLO cross sections [54]. The $t\bar{t}+W/Z$ processes are generated with MADGRAPH [55], with parton shower and hadronization performed with PYTHIA, and also normalized to NLO cross sections [56]. The W+jets samples are produced in a similar manner as the ALPGEN Z+jets samples.

The multi-jet background is estimated using data samples satisfying the nominal trigger requirements but enriched in fake leptons obtained by requiring that both leptons fail the standard identification requirements. Other requirements are applied to reduce Drell-Yan and $t\bar{t}$ contamination. The multi-jet estimate is then obtained by applying the same kinematic selection to these samples as the nominal data sample with a normalization determined at the preselection level to account for the difference between data and all other backgrounds in the dilepton mass region between 50 and 75 GeV. In both the ee and $\mu\mu$ channels, the difference is comparable or smaller than the uncertainty on all other backgrounds. No multi-jet events are predicted to pass the final event selection, but the estimate in the earlier stages of the analysis has a small influence on the data-driven Z+jets corrections described in Section 8.

7 Search Strategy

Signal events are characterized by a high-p_{T} Z boson, two or more b-jets, and additional jets and leptons. Figure 3(a) shows the predicted b-tagged jet multiplicity distribution, N_{tag}, for signal and background events with a Z boson candidate and at least two jets. The strategy of the search is to test the signal plus background hypothesis in events with $N_{\mathrm{tag}} \geq 2$, and use events with $N_{\mathrm{tag}} < 2$ as control regions to validate the modeling of the backgrounds. The $p_{\mathrm{T}}(Z)$ distribution is then studied in each N_{tag} bin ($N_{\mathrm{tag}} = 0, 1, \geq 2$), as well as the scalar sum of the p_{T} of the selected jets, $H_{\mathrm{T}}(\mathrm{jets})$. Figure 3(b) shows the $p_{\mathrm{T}}(Z)$ distribution, and Fig. 3(c) the $H_{\mathrm{T}}(\mathrm{jets})$ distribution, for signal and background events after

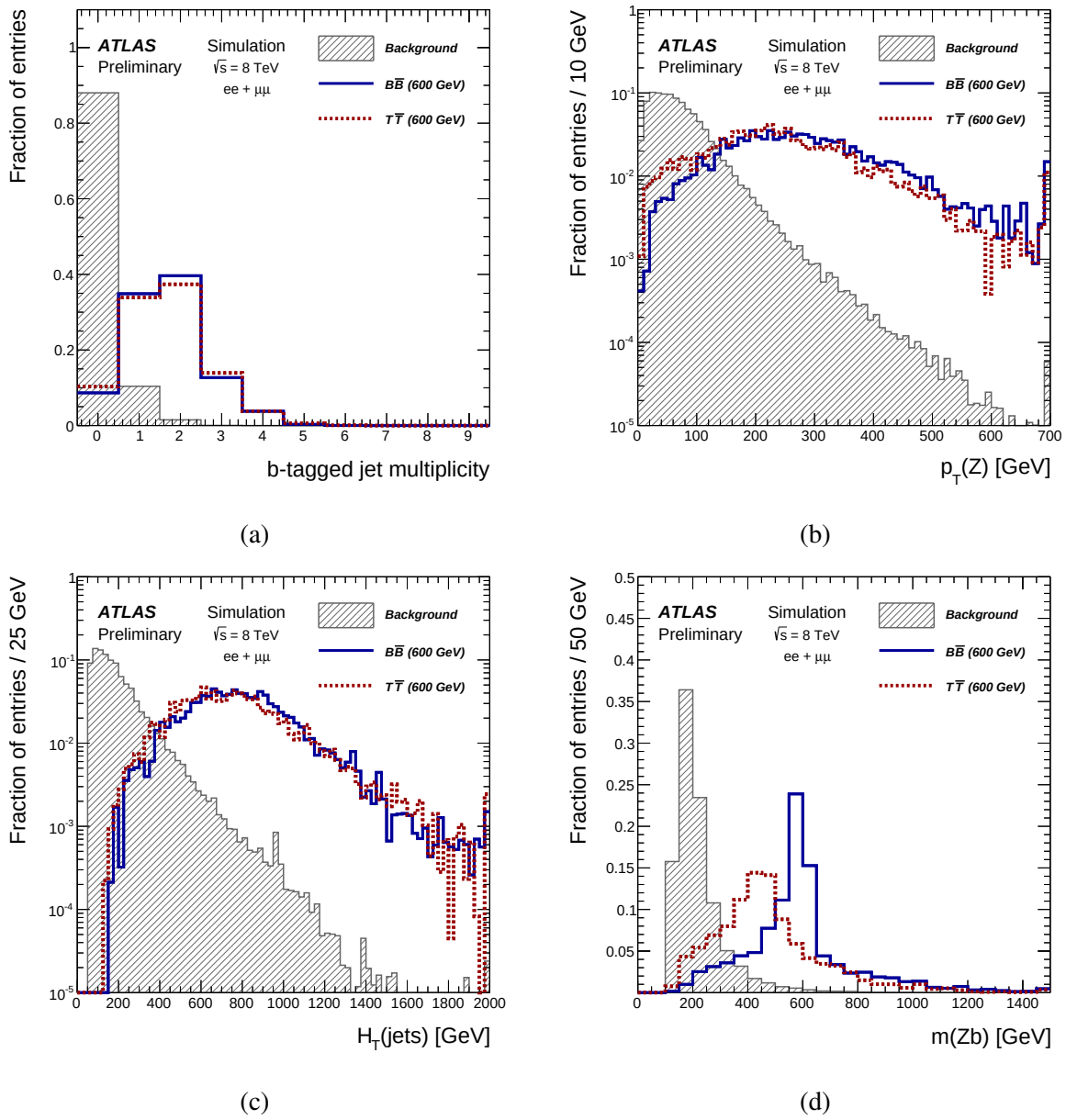

Figure 3: Unit-normalized distributions of signal-sensitive variables employed in the analysis. The filled histogram corresponds to SM backgrounds, while the dashed and solid lines correspond to the $T\bar{T}$ and $B\bar{B}$ signal, respectively, assuming a heavy quark mass of 600 GeV with vector-like singlet branching ratios. Panel (a) displays the b-tagged jet multiplicity after a $Z+\geq 2$ jets selection, while (b), (c), and (d) present the $p_{\mathrm{T}}(Z)$, $H_{\mathrm{T}}(\mathrm{jets})$, and $m(Zb)$ distributions, respectively, after a $Z+\geq 2$ b-tagged jet selection. The rightmost bin in each histogram contains overflow events.

requiring $N_{\mathrm{tag}} \geq 2$. The invariant mass of the Z boson candidate and the highest-p_{T} b-tagged jet, $m(Zb)$, is used for the hypothesis test and is shown in Fig. 3(d). The final test is performed after requiring $p_{\mathrm{T}}(Z) >$ 150 GeV and $H_{\mathrm{T}}(\mathrm{jets}) > 600$ GeV. The fraction of events of satisfying the N_{tag}, $p_{\mathrm{T}}(Z)$, and $H_{\mathrm{T}}(\mathrm{jets})$ requirements with respect to those passing the preselection of Z candidates ranges from approximately 15% (8%) to 49% (46%) for heavy quarks masses between 400 and 800 GeV assuming a $B\bar{B}$ ($T\bar{T}$) signal with $SU(2)$ singlet branching ratios.

8 Comparison of the Data to the Predictions

After preselection, the data sample consists of 3.8 million Z candidate events in the ee channel and 4.9 million events in the $\mu\mu$ channel, in agreement with the predictions within the total uncertainty, which at this stage of the analysis is dominated by the uncertainty on the Drell-Yan cross section prediction, the uncertainty on the integrated luminosity, and lepton reconstruction uncertainties. Properties of the inclusive Z candidate sample, such as the Z candidate mass and transverse momentum distributions, as well as the multiplicity distribution of selected jets, are also found to be in good agreement at this stage.

Next, the sample is restricted to Z candidate events with at least two jets, totaling 148 thousand events in the ee channel and 203 thousand events in the $\mu\mu$ channel. The predicted event yields are consistent to a degree compatible with experimental uncertainties, and consistent with a dedicated measurement of the Z+jets cross section [57]. Events are then separated according to N_{tag}, where more significant deviations are observed between data and the predictions. Such disagreements are not unexpected [58], and are accounted for as follows. The Z+jets prediction is scaled in each N_{tag} category such that the observed and predicted event yields agree in the control region $p_{\text{T}}(Z) < 100$ GeV, while the non-Z backgrounds remain fixed at their nominal predictions. The justification for scaling the Z+jets prediction and not the non-Z backgrounds, particularly in the $N_{\text{tag}} \geq 2$ category, is supported by examining the sidebands of the Z candidate mass distribution, $m(Z)$. Further, the scaling factor applied is the same for each Z+jets flavor category (i.e. bottom, charm, light). This is justified by studying a flavor sensitive variable [59], and noting that the default flavor composition in each N_{tag} bin is in reasonable agreement with data, and moderate variations of the flavor composition do not impact the final results. The scaling factors are re-computed as the impact of systematic uncertainties, such as b-tagging related uncertainties, are assessed. Figure 4(a) shows the $m(Z)$ distribution, combining the ee and $\mu\mu$ channels, for events with $N_{\text{tag}} = 1$, while Fig. 4(b) shows the same for events with $N_{\text{tag}} \geq 2$, both after applying the scaling corrections. The

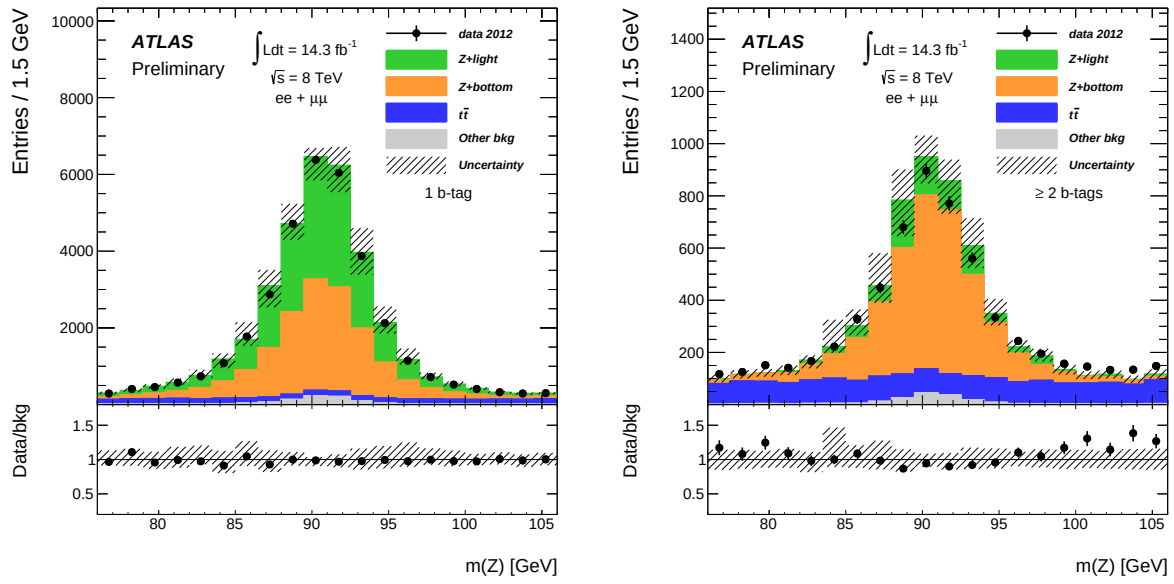

(a) (b)

Figure 4: The Z boson candidate mass distribution, $m(Z)$, in events containing at least two jets, of which (a) exactly one is b-tagged, and (b) at least two are b-tagged. The hatched bands in the upper and lower panels represent the total background uncertainty. The Z+bottom category contains events filtered for a b hadron, while the Z+light category contains events without a b hadron.

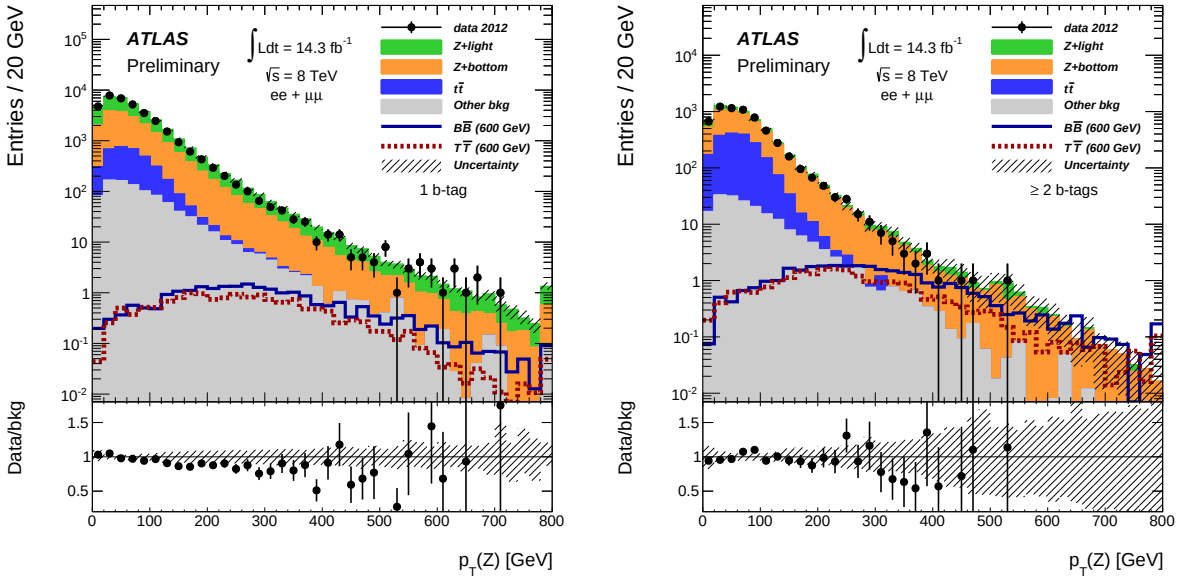

(a) (b)

Figure 5: The Z boson candidate transverse momentum distribution, $p_{\mathrm{T}}(Z)$, in events containing at least two jets, of which (a) exactly one is b-tagged, and (b) at least two are b-tagged. The Z+jets prediction in (a) is shown before the $p_{\mathrm{T}}(Z)$ correction described in the text, while in (b) it is shown after. The hatched bands in the upper and lower panels represent the total background uncertainty. The rightmost bin in each histogram contains overflow events.

scaling correction for the $N_{\mathrm{tag}} = 1$ SHERPA prediction is negligible, while the correction for $N_{\mathrm{tag}} \geq 2$ is approximately $+30\%$.

The modeling of the $p_{\mathrm{T}}(Z)$ distribution is considered next. Figure 5(a) shows the $p_{\mathrm{T}}(Z)$ distribution for the $N_{\mathrm{tag}} = 1$ sample. The SHERPA prediction is observed to increasingly over-shoot the data with increasing $p_{\mathrm{T}}(Z)$. As seen in Table 1, this trend results in a $\sim 15\%$ over-prediction of events with $p_{\mathrm{T}}(Z) > 150$ GeV, and a $\sim 30\%$ over-prediction of events satisfying, in addition, $H_{\mathrm{T}}(\mathrm{jets}) > 600$ GeV. A similar bias is observed in the $N_{\mathrm{tag}} = 0$ sample. To mitigate this bias, a reweight function parameterized by the $p_{\mathrm{T}}(Z)$ variable is derived in the $N_{\mathrm{tag}} = 1$ sample to modify the Z+jets prediction in order that the total background prediction agrees with data. The influence of the presence of signal was studied and shown to be negligible for signal strengths of interest. A similar reweight function is derived in the $N_{\mathrm{tag}} = 0$ sample to cross-check the correction and used to assign a systematic uncertainty. The background prediction in the $N_{\mathrm{tag}} = 1$ sample is also shown in Table 1 after applying the $p_{\mathrm{T}}(Z)$ correction. The final prediction for events passing the $p_{\mathrm{T}}(Z)$ and $H_{\mathrm{T}}(\mathrm{jets})$ requirements decreases from 156.4 ± 9.3 to 138.5 ± 17.5 events, and is compatible with the observed number of events in this control region. Figure 5(b) shows $p_{\mathrm{T}}(Z)$ distribution for the $N_{\mathrm{tag}} \geq 2$ sample after the $p_{\mathrm{T}}(Z)$ correction has been applied.

The $H_{\mathrm{T}}(\mathrm{jets})$ distribution is shown in Fig. 6(a) and Fig. 6(b) after applying the $p_{\mathrm{T}}(Z)$ correction and requiring $p_{\mathrm{T}}(Z) > 150$ GeV in events with $N_{\mathrm{tag}} = 1$ and $N_{\mathrm{tag}} \geq 2$, respectively. The data are well modeled by the SM background prediction in the $N_{\mathrm{tag}} = 1$ control region over the full range of $H_{\mathrm{T}}(\mathrm{jets})$ values. Therefore, the final $H_{\mathrm{T}}(\mathrm{jets}) > 600$ GeV requirement is applied. Figure 7(a) and Fig. 7(b) show the final $m(Zb)$ distribution for the $N_{\mathrm{tag}} = 1$ control region and $N_{\mathrm{tag}} \geq 2$ signal region, respectively. Figures 12 and 13 of Appendix A present the same distributions separated according to lepton final state. Table 2 provides the predicted and observed event yields for the $N_{\mathrm{tag}} \geq 2$ sample.

Although the detailed comparison between data and the SM background has been presented using the

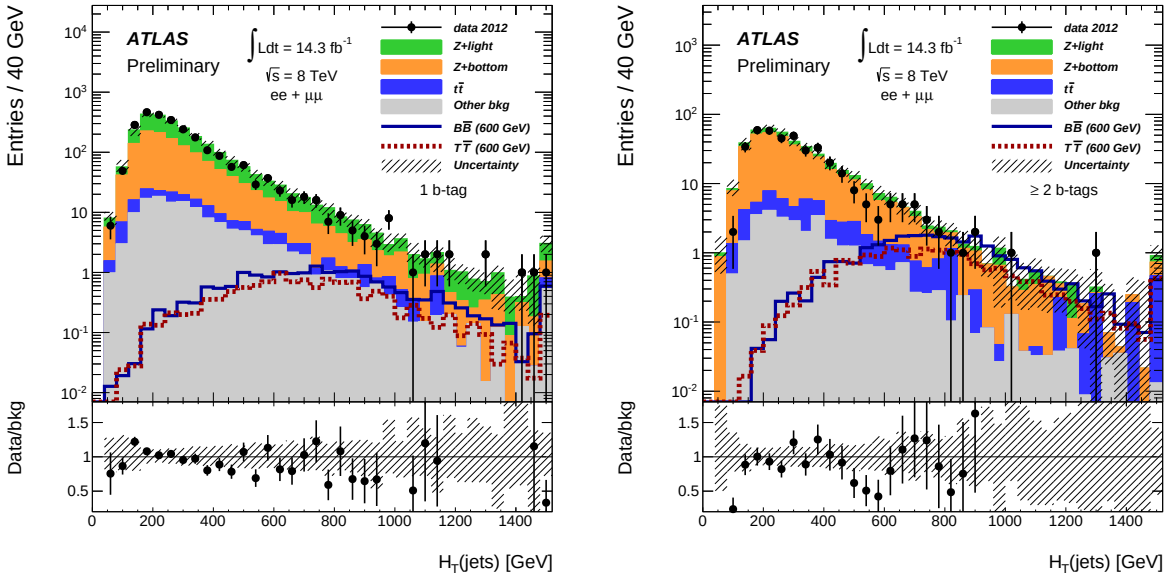

(a) (b)

Figure 6: The $H_{\mathrm{T}}(\mathrm{jets})$ jets distribution after requiring $p_{\mathrm{T}}(Z) > 150$ GeV, in Z candidate events containing at least two jets, of which (a) exactly one is b-tagged, and (b) at least two are b-tagged. The Z+jets predictions in (a) and (b) are shown after the $p_{\mathrm{T}}(Z)$ correction described in the text. The hatched bands in the upper and lower panels represent the total background uncertainty. The rightmost bin in each histogram contains overflow events.

SHERPA prediction, consistent results are obtained using the ALPGEN prediction when similarly derived corrections are applied, albeit with reduced statistical precision in the final stages of event selection.

9 Systematic Uncertainties

Several sources of systematic uncertainty affect the predicted SM backgrounds and signal, and the distribution of each in $m(Zb)$ after the final selection. The sources of uncertainty are described below and assumed to be uncorrelated. The impact is evaluated by propagating each uncertainty through the full analysis chain for each signal or background source, and allowing the final predictions to vary accordingly during hypothesis testing. Table 3 lists the fractional uncertainty in the normalization of the final signal and background predictions for each category of systematic uncertainty.

9.1 Luminosity

The uncertainty on the integrated luminosity is 3.6% [34], resulting in a normalization uncertainty on processes estimated with simulated samples. In addition, since the Z+jets background prediction is corrected to account for differences between data and all other backgrounds in control regions, the luminosity uncertainty also indirectly impacts the yield of this background source as well.

9.2 Signal and background cross sections

Uncertainty in signal and background cross sections results in a normalization uncertainty on processes estimated with simulation. As above, SM background cross section uncertainties [35, 51, 54, 56] indi-

Table 1: Predicted and observed number of events after selecting a Z boson candidate and at least two jets, exactly one of which is b-tagged. The number of events further satisfying $p_{\mathrm{T}}(Z) > 150$ GeV is listed next, followed by the number satisfying, in addition, $H_{\mathrm{T}}(\mathrm{jets}) > 600$ GeV. SM background yields are listed by category, as well as combined. The Z+jets predictions, as well as the total background prediction, are shown before and after the $p_{\mathrm{T}}(Z)$ correction described in the text. Reference $B\bar{B}$ and $T\bar{T}$ signal yields are provided for $m_{B/T} = 600$ GeV and $SU(2)$ singlet branching ratios.

	$Z+ \geq 2$jets ($N_{tag} = 1$)	$p_{\mathrm{T}}(Z) > 150$ GeV	$H_{\mathrm{T}}(\mathrm{jets}) > 600$ GeV
Z+light (before p_{T} corr.)	$17,000 \pm 1,200$	$1,370 \pm 150$	78.3 ± 5.9
Z+light (after p_{T} corr.)	$16,700 \pm 1,500$	$1,170 \pm 190$	68 ± 15
Z+bottom (before p_{T} corr.)	$15,000 \pm 1,400$	$1,290 \pm 170$	56.3 ± 5.0
Z+bottom (after p_{T} corr.)	$14,700 \pm 1,400$	$1,110 \pm 180$	49 ± 11
$t\bar{t}$	$2,700 \pm 300$	60.7 ± 8.8	7.8 ± 2.1
Other SM	900 ± 300	135 ± 45	14.0 ± 5.2
Total SM (before p_{T} corr.)	$35,600 \pm 2,000$	$2,850 \pm 230$	156.4 ± 9.3
Total SM (after p_{T} corr.)	$35,000 \pm 2,000$	$2,470 \pm 270$	139 ± 20
Data	34,955	2,480	121
$B\bar{B}$ ($m_B = 600$ GeV)	22.5 ± 3.4	18.7 ± 2.9	13.0 ± 2.4
$T\bar{T}$ ($m_T = 600$ GeV)	15.2 ± 2.1	12.0 ± 1.6	8.0 ± 1.3

Table 2: Predicted and observed events after selecting a Z boson candidate and at least two jets, at least two of which are b-tagged. The number of events further satisfying $p_{\mathrm{T}}(Z) > 150$ GeV is listed next, followed by the number satisfying, in addition, $H_{\mathrm{T}}(\mathrm{jets}) > 600$ GeV. SM background yields are listed by category, as well as combined. The Z+jets prediction is shown after the $p_{\mathrm{T}}(Z)$ correction described in the text. Reference $B\bar{B}$ and $T\bar{T}$ signal yields are provided for $m_{B/T} = 600$ GeV and $SU(2)$ singlet branching ratios.

	$Z+ \geq 2$jets ($N_{tag} \geq 2$)	$p_{\mathrm{T}}(Z) > 150$ GeV	$H_{\mathrm{T}}(\mathrm{jets}) > 600$ GeV
Z+light	850 ± 240	58 ± 17	4.3 ± 1.8
Z+bottom	3380 ± 470	301 ± 55	17.8 ± 4.8
$t\bar{t}$	1730 ± 320	31.1 ± 6.2	5.1 ± 1.4
Other SM	190 ± 60	29.2 ± 7.0	3.0 ± 1.2
Total SM	$6,150 \pm 620$	419 ± 59	30.2 ± 5.3
Data	6,097	386	26
$B\bar{B}$ ($m_B = 600$ GeV)	31.0 ± 4.3	25.7 ± 3.6	19.8 ± 2.7
$T\bar{T}$ ($m_T = 600$ GeV)	21.9 ± 2.8	17.1 ± 2.2	12.2 ± 1.7

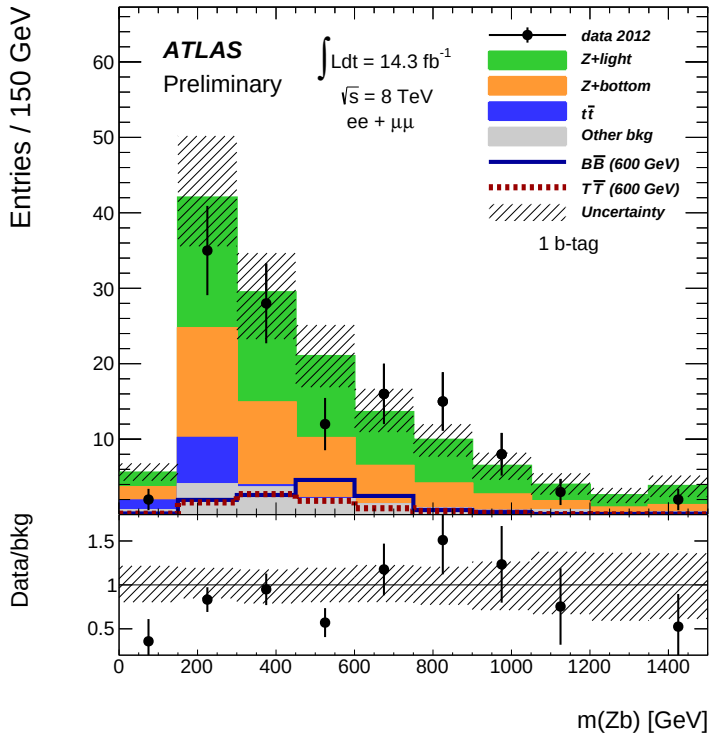

(a)

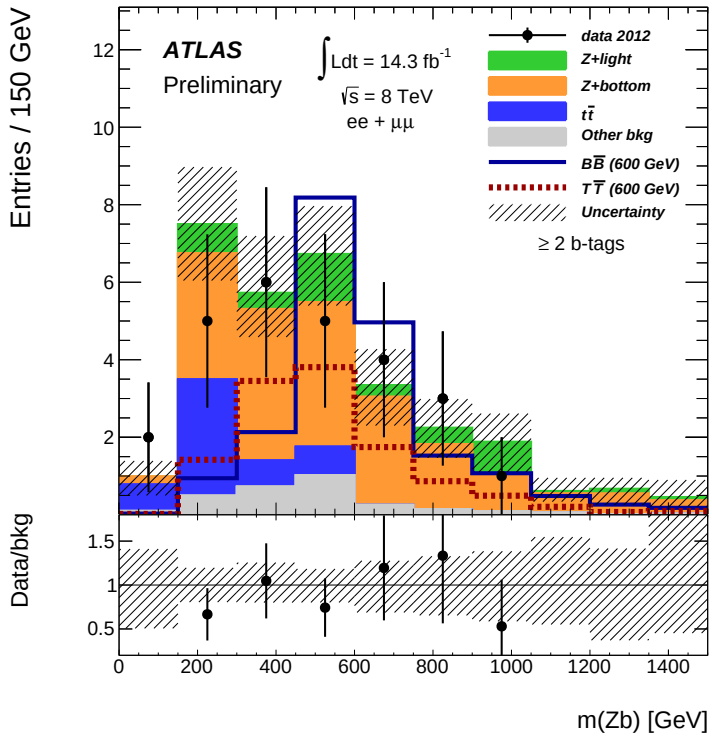

(b)

Figure 7: The $m(Zb)$ distribution after the $p_{\mathrm{T}}(Z)$ and $H_{\mathrm{T}}(\mathrm{jets})$ requirements, in Z candidate events containing at least two jets, of which (a) exactly one is b-tagged, and (b) at least two are b-tagged. The hatched bands in the upper and lower panels represent the total background uncertainty. The rightmost bin in each histogram contains overflow events.

Table 3: The fractional uncertainties (%) in the yields of signal and background events after the final selection. The uncertainties are grouped into categories that are explained in more detail in the text.

	$Z+$ jets	$t\bar{t}$	Other bkg.	$B\bar{B}$ (600 GeV)	$T\bar{T}$ (600 GeV)
Luminosity	1.7	3.6	3.6	3.6	3.6
Cross section	7.0	11	28	-	-
Jet Reco.	12	14	15	4.8	5.8
b-tagging	7.1	13	13	11	10
e Reco.	1.8	6.8	3.0	3.9	3.8
μ Reco.	1.8	2.3	4.9	4	4.2
$Z+$ jets rate corr.	9.1	–	–	–	–
$Z+$ jets $p_{\mathrm{T}}(Z)$ corr.	19	–	–	–	–

rectly influence the normalization of the Z+jets background prediction. Uncertainties in the signal cross section are not included during hypothesis testing.

9.3 Jet reconstruction

9.3.1 Jet energy scale

The jet energy scale [32] was determined using information from test-beam data, LHC collision data, and simulation. The corresponding uncertainty varies between 2.5% and 8%, depending on the p_{T} and η of selected jets in this analysis. Additional uncertainties associated with other pp interactions in the same bunch crossing can be as large as 5%. Likewise, an additional uncertainty of up to 2.5%, depending on the p_{T} of the jet, is applied for b-jets.

9.3.2 Jet energy resolution

The energy resolution of jets was measured in dijet events and agrees with predictions from simulations within 10%, and the corresponding uncertainty is evaluated by smearing the jet energy accordingly.

9.3.3 Jet reconstruction efficiency

The jet reconstruction efficiency was estimated using minimum bias and QCD dijet events. The inefficiency was found to be at most 2.7% for low p_{T} and at the per mill level for high p_{T} jets. This uncertainty is taken into account by randomly removing jets in simulated events.

9.3.4 Jet Vertex Fraction cut

A requirement on the jet vertex fraction variable is made to reduce the impact of pile-up jets (jets from other pp interactions in the same bunch crossing). The performance of this requirement was compared in data and simulation for $Z(\rightarrow \ell^+\ell^-)+1$-jet events, selecting separately events enriched in hard-scatter jets and events enriched in pile-up jets. Simulation correction factors were determined separately for both types. For hard-scatter jets they decrease from ~ 1.03 at $p_{\mathrm{T}} = 25$ GeV to ~ 1.01 at $p_{\mathrm{T}} > 50$ GeV, while for pile-up jets they are consistent with unity. The product of per-jet scale factor uncertainties results in an overall uncertainty on the signal and background acceptance of less than 4%.

9.4 b-tagging of jets

Dedicated performance studies of the b-tagging algorithm have been performed and calibration factors determined [60, 61, 62]. Efficiencies for tagging b-jets (c-jets) in simulation are corrected by p_{T} and η-dependent factors in the range 0.9–1.0 (1.1-1.2), whereas the light jet efficiency is corrected by a factor of ~ 1.3. The uncertainties in these corrections are between 7% and 13% for b-jets, 15% and 39% for c-jets, and $\sim 25\%$ for light jets.

9.5 Lepton reconstruction and trigger

9.5.1 Lepton identification, reconstruction, and trigger

The uncertainties on the identification and reconstruction efficiency of electrons and muons, as well as the efficiency of the single lepton triggers used in the analysis, affect the nominal scale factors used to correct differences observed between data and simulation. When combined, these lepton efficiency uncertainties contribute to an uncertainty on the final signal and background estimates at the level of 5%.

9.5.2 Lepton momentum scale and resolution

Data events with leptonic decays of the Z boson were used to measure the lepton momentum scale and resolution, and simulation correction factors with associated uncertainties were derived. The effect of momentum scale uncertainties were evaluated by repeating the event selection with the electron and muon momentum varied according to the corresponding uncertainties. The impact of the momentum resolution uncertainty was evaluated by smearing the lepton momentum in simulation accordingly. The lepton momentum uncertainties contribute to an uncertainty on the final signal and background estimates at the level of 1%.

9.6 Systematics associated with data-driven Z+jets corrections

The Z+jets scaling factor and the $p_{\mathrm{T}}(Z)$ shape correction are derived in control regions and applied to the signal region. The rate correction was derived in both the $p_{\mathrm{T}}(Z) < 100$ GeV and the $50 < p_{\mathrm{T}}(Z) < 150$ GeV regions and the difference in the resulting predictions was used to assess an uncertainty. Similarly, the $p_{\mathrm{T}}(Z)$ shape correction was derived in both the $N_{\mathrm{tag}} = 0$ and $N_{\mathrm{tag}} = 1$ control regions, and the difference when applied to the $N_{\mathrm{tag}} \geq 2$ signal region used to assign an uncertainty. The dominant uncertainty in this correction, however, is the statistical uncertainty associated with the baseline correction function derived in the $N_{\mathrm{tag}} = 1$ control region.

10 Final Results

In the absence of a signal-like excess of events in the final $m(Zb)$ distribution presented in Fig. 7(b), upper limits at the 95% confidence level (C.L.) are derived on the pair production cross section of vector-like quarks with masses between 350 and 850 GeV. A binned Poisson likelihood test of the final $m(Zb)$ distribution is performed. The test employs a log-likelihood ratio function, $-2\log(L_{\mathrm{s+b}}/L_{\mathrm{b}})$, where $L_{\mathrm{s+b}}$ (L_{b}) is the Poisson probability to observe data under the signal plus background (background only) hypothesis. Pseudo-experiments are performed incorporating the impact of systematic uncertainties, and limits are derived according to the CL_{s} method [63, 64].

Figure 8(a) presents the cross section limit versus mass on the pair production of an $SU(2)$ singlet vector-like B quark, while Fig. 8(b) presents the same for a vector-like B quark that is part of an $SU(2)$ (B,Y) doublet with a charge $-4/3$ Y quark. In the former case, the observed (expected) mass limit is 645 GeV (635 GeV), while in the latter case the observed (expected) mass limit is 725 GeV (720 GeV).

Figure 9(a) presents the cross-section limit versus mass on the pair production of an $SU(2)$ singlet vector-like T quark, while Fig. 9(b) presents the same for a vector-like T quark that is part of an $SU(2)$ doublet. In the former case, the observed (expected) mass limit is 585 GeV (550 GeV), while in the latter case the observed (expected) mass limit is 680 GeV (660 GeV).

Figure 10 presents exclusion limits at 95% C.L. for the $B\bar{B}$ hypothesis in the (Wt,Hb) branching ratio plane for B masses between 350-850 GeV. Similarly, Fig. 11 presents exclusion limits at 95% C.L. for the $T\bar{T}$ hypothesis in the (Wb,Ht) branching ratio plane for T masses between 350-850 GeV.

11 Summary

A search has been reported for the pair production of a new heavy quark with its antiparticle, assuming the new quark has a significant branching ratio to decay into a Z boson and a third generation SM quark. The data analyzed correspond to 14.3 fb^{-1} of pp collisions at $\sqrt{s} = 8$ TeV recorded in 2012 with the ATLAS detector at the CERN LHC. Selected events contain a high transverse momentum Z boson candidate reconstructed from a pair of oppositely charged electrons or muons, at least two jets possessing properties consistent with the hadronization of a b quark, as well as large total transverse momentum of all central jets in the event. No significant excess of events above the SM expectation is observed, and upper limits are derived for vector-like quarks of various masses.

In the case of a charge $+2/3$ vector-like T quark, a mass lower than 585 GeV is excluded at the 95% C.L. under branching ratio assumptions corresponding to a weak-isospin singlet, while a mass lower than 680 GeV is excluded at the 95% C.L under branching ratio assumptions corresponding to a T quark in a (T,B) doublet. The corresponding limits derived in a $T \to Ht$ targeted search [25] are 640 GeV and 790 GeV, respectively. Although the limits are weaker in the present analysis under these assumptions, the limits are extended when arbitrary branching ratios are considered, in particular for low $BR(T \to Ht)$.

In the case of a charge $-1/3$ vector-like B quark, a mass lower than 645 GeV is excluded at the 95% C.L. under branching ratio assumptions corresponding to a weak-isospin singlet, while a mass lower than 725 GeV is excluded at the 95% C.L. under branching ratio assumptions corresponding to a B quark in a (B,Y) doublet. The former limit represents an improvement upon the 590 GeV limit derived in a general search for same-sign dileptons and b-jets [22] whose sensitivity is largest for large values of $BR(B \to Wt)$. This search considerably extends the mass limits under arbitrary branching ratio assumptions, in particular for low $BR(B \to Wt)$. The latter limit on a B quark in a (B,Y) doublet is the first such interpretation and of particular interest in light of a recent paper [18].

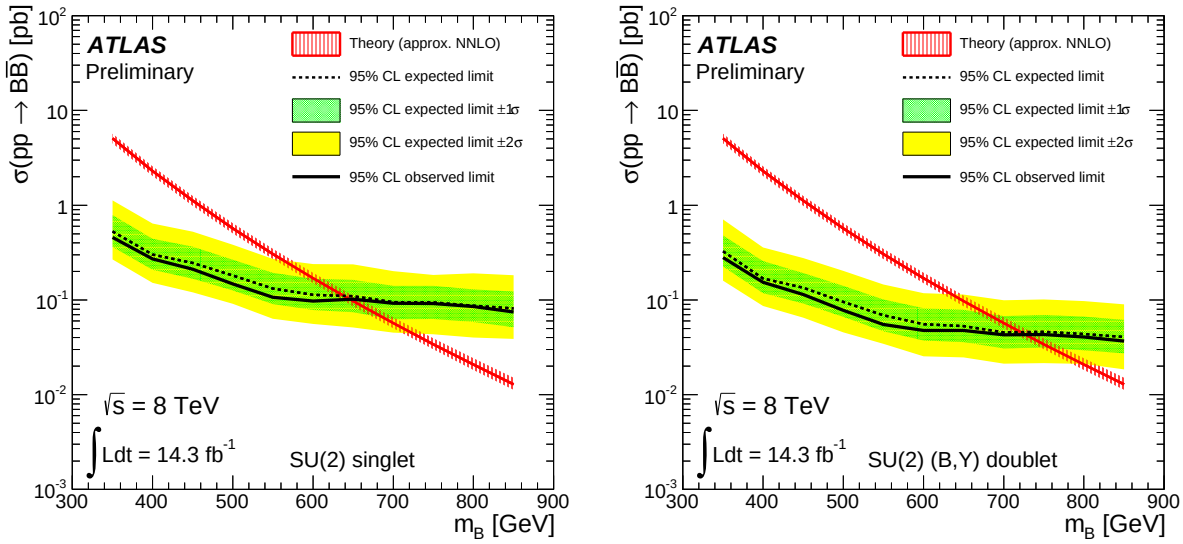

(a) (b)

Figure 8: Pair production cross section limit (95% C.L.) versus mass for (a) a $SU(2)$ singlet vector-like B quark, and (b) a vector-like B quark forming an $SU(2)$ (B,Y) doublet with a charge $-4/3$ Y quark.

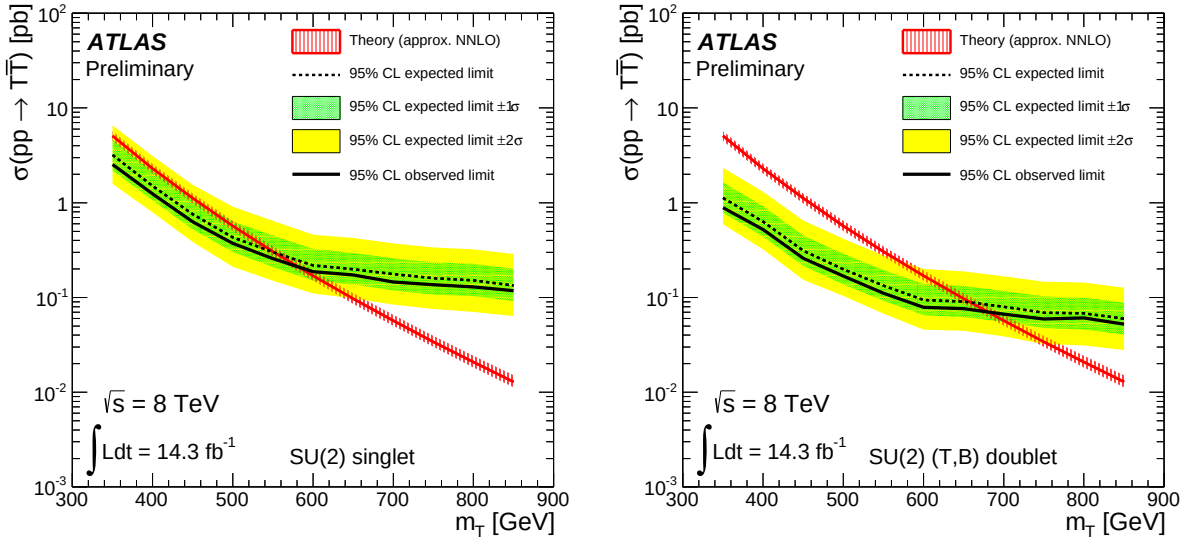

(a) (b)

Figure 9: Pair production cross section limit (95% C.L.) versus mass for (a) a $SU(2)$ singlet vector-like T quark, and (b) a vector-like T quark forming an $SU(2)$ (T,B) doublet with a charge $-1/3$ B quark.

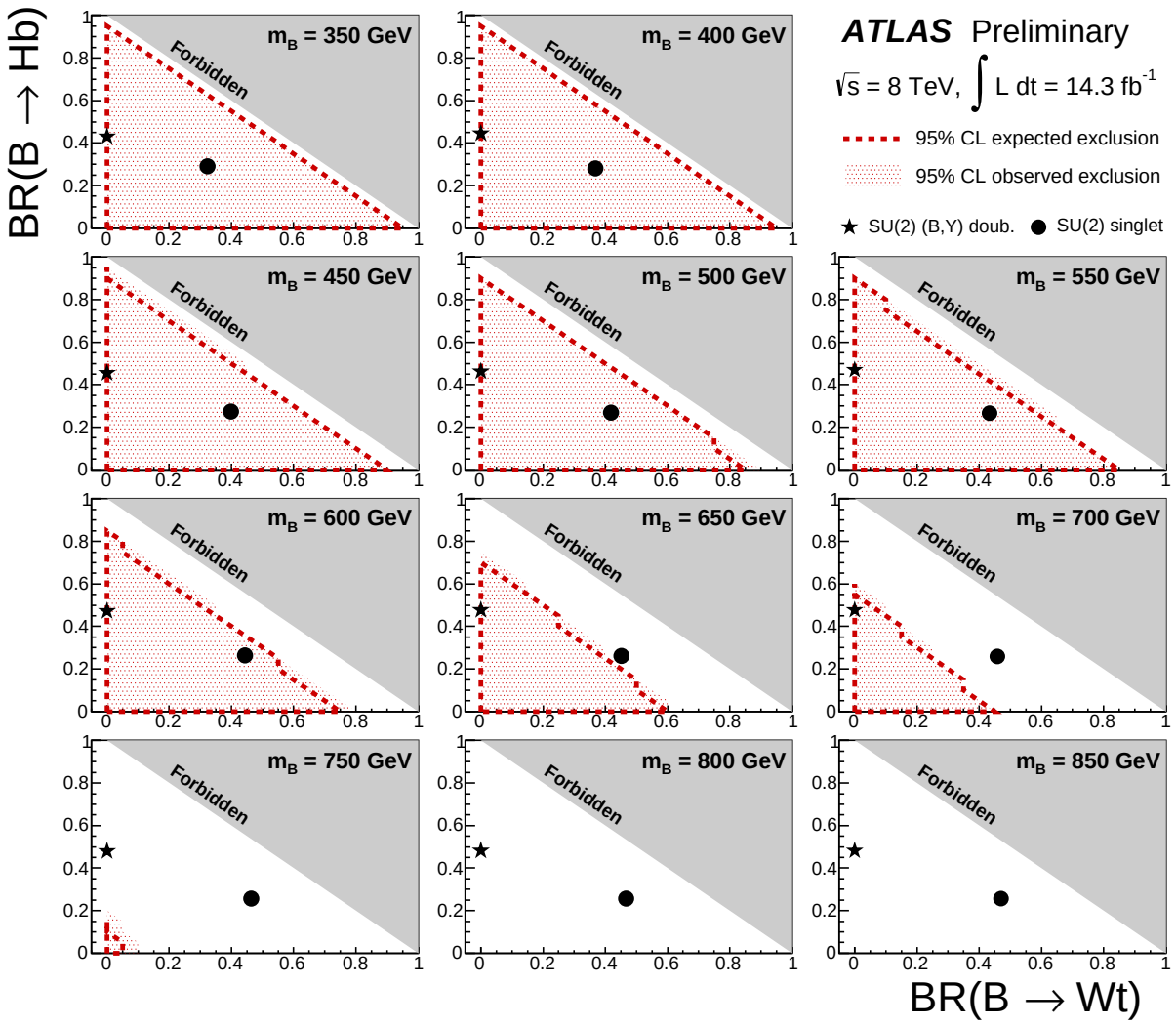

Figure 10: Exclusion limits at 95% C.L. for the $B\bar{B}$ pair production hypothesis in the (Wt, Hb) branching ratio plane for B masses between 350-850 GeV.

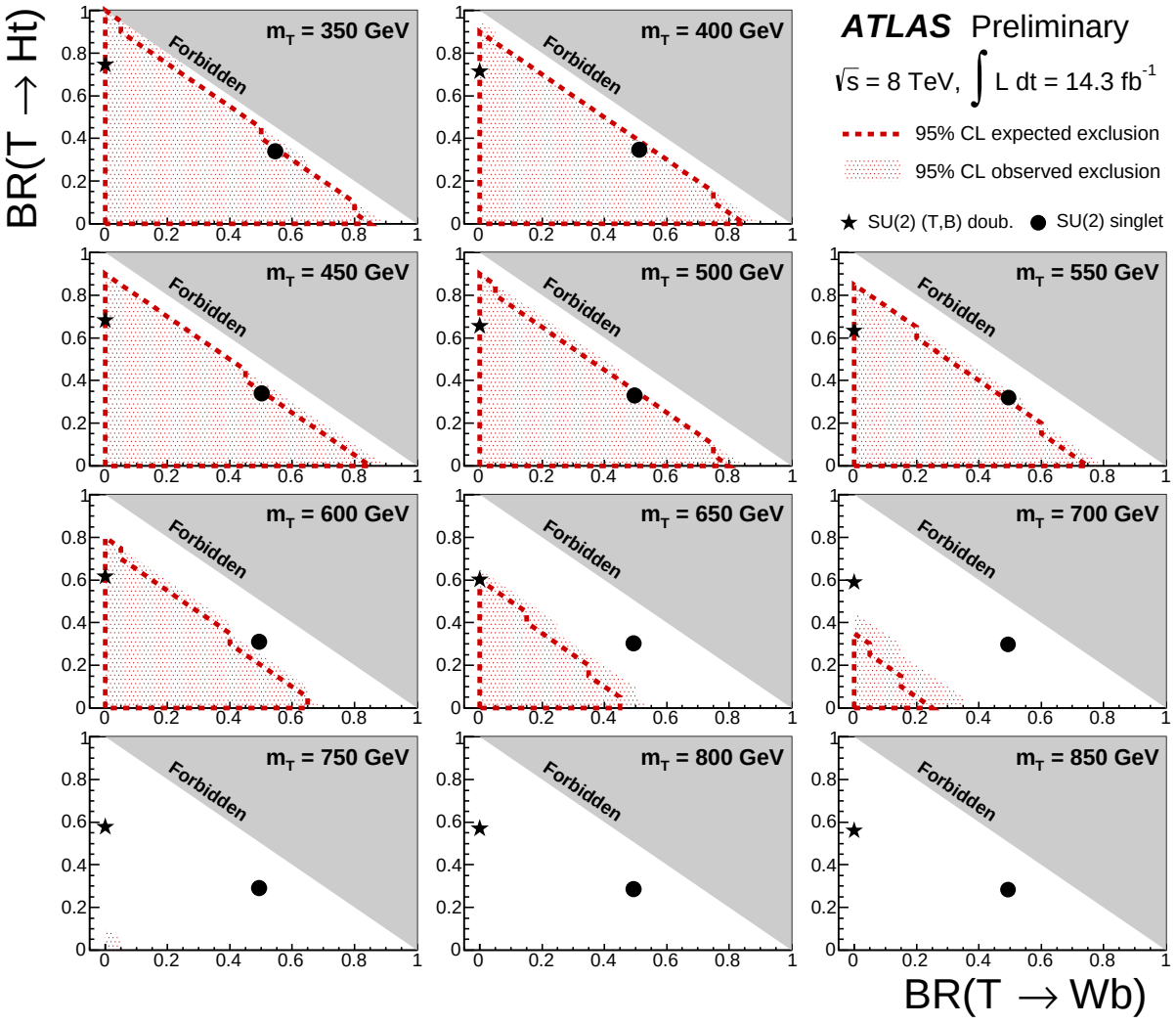

Figure 11: Exclusion limits at 95% C.L. for the $T\bar{T}$ pair production hypothesis in the (Wb, Ht) branching ratio plane for T masses between 350-850 GeV.

References

[1] The ALEPH, DELPHI, L3, OPAL, SLD Collaborations, the LEP Electroweak Working Group, the SLD Electroweak and Heavy Flavor Groups, *Precision Electroweak Measurements on the Z Resonance*, Phys. Rept. **427** (2006) 257, hep-ex/0509008.

[2] The ALEPH, DELPHI, L3, OPAL Collaborations, the LEP Electroweak Working Group, *Electroweak Measurements in Electron-Positron Collisions at W-Boson-Pair Energies at LEP*, CERN-PH-EP-2013-022 (2013), submitted to Phys. Rept., arXiv:1302.3415.

[3] ATLAS Collaboration, *Observation of a new particle in the search for the Standard Model Higgs boson with the ATLAS detector at the LHC*, Phys. Lett. B **706** (2012) 1, arXiv:1207.7214.

[4] CMS Collaboration, *Observation of a new boson at a mass of 125 GeV with the CMS experiment at the LHC*, Phys. Rev. Lett. **108** (2012) 261802, arXiv:1207.7235.

[5] K. Wilson, as quoted in L. Susskind, *Dynamics of spontaneous symmetry breaking in the Weinberg-Salam theory*, Phys. Rev. D **20** (1979) 2619.

[6] P. Ramond, *Dual Theory for Free Fermions*, Phys. Rev. D **3** (1971) 2415. Yu. Gol'fand and E.P. Likhtman, *Extension of the Algebra of Poincare Group Generators and Violation of p Invariance*, JETP Lett. **13** (1971), 323. J. Wess and B. Zumino, *A Langrangian Model Invariant Under Supergauge Transformations*, Phys. Lett. B **49** (1974), 52. P. Fayet, *Supersymmetry and Weak, Electromagnetic and Strong Interactions*, Phys. Lett. B **64** (1976), 159.

[7] ATLAS Collaboration, *Search for direct production of the top squark in the all-hadronic $t\bar{t}$ plus missing transverse energy final state in* 21 fb^{-1} *of pp collisions at* $\sqrt{s} = 8$ *TeV with the ATLAS detector*, ATLAS-CONF-2013-024. ATLAS Collaboration, *Search for direct production of charginos and neutralinos in events with three leptons and missing transverse momentum in* 21 fb^{-1} *of pp collisions at* $\sqrt{s} = 8$ *TeV with the ATLAS detector*, ATLAS-CONF-2013-035. ATLAS Collaboration, *Search for squarks and gluinos with the ATLAS detector in final states with jets and missing transverse momentum and* 20.3 fb^{-1} *of* $\sqrt{s} = 8$ *TeV collision data*, ATLAS-CONF-2013-047.

[8] C. T. Hill and E. H. Simmons, *Strong Dynamics and Electroweak Symmetry Breaking*, Phys. Rept. **381** (2003) 235, Erratum-ibid. **390** (2004) 553, arXiv:hep-ph/0203079.

[9] C. T. Hill, *Topcolor Assisted Technicolor*, Phys. Lett. B **345** (1995) 483. B. A. Dobrescu and C. T. Hill, *Electroweak Symmetry Breaking via Top Condensation Seesaw*, Phys. Rev. Lett. **81** (1998) 2634.

[10] N. Arkani-Hamed, A.G. Cohen, E. Katz, and A. E. Nelson, JHEP **0207** (2002) 034, arXiv:hep-ph/0206021.

[11] For a review see M. Schmalz and D. Tucker-Smith, *Little Higgs review*, Ann. Rev. Nucl. Sci. **55**, (2005) 229, arXiv:hep-ph/0502182.

[12] R. Contino, Y. Nomura and A. Pomarol, *Higgs as a holographic pseudoGoldstone boson*, Nucl. Phys. B **671** (2003) 148, arXiv:hep-ph/0306259; K. Agashe, R. Contino and A. Pomarol, *Pseudo-goldstone higgs from five dimensions*, Nucl. Phys. B **719** (2005) 165, arXiv:hep-ph/0412089; R. Contino, L. Da Rold and A. Pomarol, *Light custodians in natural composite Higgs model*, Phys. Rev. D **75** (2007) 055014, arXiv:hep-ph/0612048.

[13] F. del Aguila, M. Perez-Victoria and J. Santiago, *Observable contributions of new exotic quarks to quark mixing*, JHEP **09** (2000) 011, arXiv:hep-ph/0007316.

[14] J. Berger, J. Hubisz, M. Perelstein, *A Fermionic Top Partner: Naturalness and the LHC*, JHEP **07** (2012) 016, arXiv:1205.0013.

[15] R. Contino and G. Servant, *Discovering the top partners at the LHC using same-sign dilepton final states*, JHEP **06** (2008) 026, arXiv:0801.1679.

[16] J. A. Aguilar-Saavedra, *Identifying Top Partners at the LHC*, JHEP **11** (2009) 030, arXiv:0907.3115.

[17] A. De Simone, O. Matsedonskyi, R. Rattazzi, A. Wulzer, *A First Top Partner's Hunter Guide*, JHEP **04** (2013) 004, arXiv:1211.5663.

[18] J.A. Aguilar-Saavedra, R. Benrik, S. Heinemeyer, M. Perez-Victoria, *A handbook of vector-like quarks: mixing and single production*, arXiv:1306.0572.

[19] S.L. Glashow, J. Iliopoulos, and L. Maiani, *Weak Interactions with Lepton-Hadron Symmetry*, Phys. Rev. D **2** (1970), 1285.

[20] F. del Aguila, L. Ametller, G. L. Kane and J. Vidal, *Vector Like Fermion And Standard Higgs Production At Hadron Colliders*, Nucl. Phys. B **334** (1990) 1;

[21] ATLAS Collaboration, *Search for pair production of heavy top-like quarks decaying to a high-p_{T} W boson and a b quark in the lepton plus jets final state at $\sqrt{s} = 7$ TeV with the ATLAS detector*, Phys. Lett. B **718** (2013) 1284, arXiv:1210.5468.

[22] ATLAS Collaboration, *Search for anomalous production of events with same-sign dileptons and b jets in* 14.3 fb^{-1} *of pp collisions at $\sqrt{s} = 8$ TeV with the ATLAS detector*, ATLAS-CONF-2013-051, http://cds.cern.ch/record/1547567.

[23] CMS Collaboration, *Search for a Vectorlike Quark with Charge 2/3 in $t + Z$ Events from pp Collisions at $\sqrt{s} = 7$ TeV*, Phys. Rev. Lett. **107** (2011) 271802, arXiv:1109.4985.

[24] ATLAS Collaboration, *Search for Pair Production of a New b' Quark that Decays into a Z Boson and a Bottom Quark with the ATLAS Detector*, Phys. Rev. Lett. **109** (2012) 071801, arXiv:1204.1265.

[25] ATLAS Collaboration, *Search for heavy top-like quarks decaying to a Higgs boson and a top quark in the lepton plus jets final state in pp collisions at t $\sqrt{s} = 8$ TeV with the ATLAS detector*, ATLAS-CONF-2013-018.

[26] ATLAS Collaboration, *The ATLAS Experiment at the CERN Large Hadron Collier*, JINST **3** (2008) S08003.

[27] ATLAS Collaboration, *Electron performance measurements with the ATLAS detector using the 2010 LHC proton-proton collision data*, Eur. Phys. J. C **72** (2012) 1909, arXiv:1110.3174.

[28] M. Cacciari, G. P. Salam and G. Soyez, *The anti-k_t jet clustering algorithm*, JHEP **04** (2008) 063, arXiv:0802.1189.

[29] M. Cacciari and G. P. Salam, *Dispelling the N^3 myth for the k_t jet-finder*, Phys. Lett. B **641** (2006) 57, arXiv:hep-ph/0512210.

[30] M. Cacciari, G. P. Salam and G. Soyez, *FastJet User Manual*, Eur. Phys. J. C **72** (2012) 1896, arXiv:1111.6097.

[31] T. Barillari *et al.*, *Local hadronic calibration*, ATL-LARG-PUB-2009-001 (2009), http://cds.cern.ch/record/1112035.

[32] ATLAS Collaboration, *Jet energy measurement with the ATLAS detector in proton-proton collisions at* $\sqrt{s} = 7$ *TeV*, submitted to Eur. Phys. J., arXiv:1112.6426.

[33] ATLAS Collaboration, *Commissioning of the ATLAS high-performance b-tagging algorithms in 7 TeV collision data*, ATLAS-CONF-2011-102, http://cds.cern.ch/record/1369219.

[34] ATLAS Collaboration, *Improved luminosity determination in pp collisions at* $\sqrt{s} = 7$ *TeV using the ATLAS detector at the LHC*, arXiv:1302.4393, submitted to EPJC.

[35] M. Aliev *et al.*, *HATHOR: a HAdronic Top and Heavy quarks crOss section calculatoR*, Comput. Phys. Commun. **182** (2011) 1034, arXiv:1007.1327.

[36] A. D. Martin *et al.*, *Parton distributions for the LHC*, Eur. Phys. J. C **63** (2009) 189, arXiv:0901.0002.

[37] A. D. Martin *et al.*, *Uncertainties of* α_s *in global PDF analyses and implications for predicted hadronic cross sections*, Eur. Phys. J. C **64** (2009) 653, arXiv:0905.3531.

[38] F. del Aguila and M. J. Bowick, *The Possibility Of New Fermions With Delta I = 0 Mass*, Nucl. Phys. B **224** (1983) 107.

[39] J. A. Aguilar-Saavedra, *Protos - PROgram for TOp Simulations*, http://jaguilar.web.cern.ch/jaguilar/protos.

[40] T. Sjostrand, S. Mrenna, P.Z. Skands, *PYTHIA 6.4 Physics and Manual*, JHEP **0605** (2006) 026, arXiv:hep-ph/0603175.

[41] Wolfgang Lukas, *Fast Simulation for ATLAS: Atlfast-II and ISF*, J. Phys. Conf. Ser. **396** 022031 (2012).

[42] ATLAS Collaboration, *The ATLAS Simulation Infrastructure*, Eur. Phys. J **C70** (2010) 823-874, arXiv:1005.4568.

[43] M. L. Mangano *et al.*, *Alpgen, a generator for hard multiparton processes in hadronic collisions*, JHEP **07** (2003) 001, arXiv:hep-ph/0206293.

[44] T. Gleisberg *et al.*, *Event generation with SHERPA 1.1*, JHEP **02** (2009) 007, arXiv:0811.4622.

[45] S. Catani, L. Cieri, G. Ferrera, D. de Florian, M. Grazzini, Phys. Rev. Lett. **103** (2009) 082001, arXiv:0903.2120.

[46] J. Pumplin *et al,*, *New generation of parton distributions with uncertainties from global QCD analysis*, JHEP **07** (2002) 012, arXiv:hep-ph/0201195.

[47] M. L. Mangano *et al.*, *Multijet matrix elements and shower evolution in hadronic collisions:* $Wb\bar{b}+$ *n jets as a case study*, Nucl. Phys. **B632** (2002) 343, arXiv:hep-ph/0108069.

[48] H.-L. Lai *et al.*, *New parton distributions for collider physics*, Phys. Rev. D **82** (2010) 074024, arXiv:1007.2241.

[49] S. Frixione, *Matching NLO QCD computations with Parton Shower simulations: the POWHEG method*, JHEP **0711** (2007) 070, arXiv:0709.2092.

[50] G. Corcella, I. G. Knowles, G. Marchesini, S. Moretti, K. Odagiri, P. Richardson, M. H. Seymour and B. R. Webber, *HERWIG 6.5 release note*, arXiv:hep-ph/0210213.

[51] J. Campbell and R. Ellis, *An update on vector boson pair production at hadron colliders*, Phys. Rev. **D60** (1999) 113006, arXiv:hep-ph/9905386.

[52] S. Frixione and B. R. Webber, *Matching NLO QCD computations and parton shower simulations*, JHEP **06** (2002) 029 arXiv:hep-ph/0204244.

[53] B. P. Kersevan and E. Richter-Was, *The Monte Carlo event generator AcerMC version 2.0 with interfaces to PYTHIA 6.2 and HERWIG 6.5*, arXiv:hep-ph/0405247.

[54] N. Kidonakis, *Differential and total cross sections for top pair and single top production*, arXiv:1205.3453.

[55] J. Alwall, P. Demin, S. de Visscher, R. Frederix, M. Herquet, F. Maltoni, T. Plehn and D. L. Rainwater *MadGraph/MadEvent v4: The New Web Generation*, JHEP **09** (2007) 028, arXiv:0706.2334.

[56] M. V. Garzelli, A. Kardos, C. G. Papadopoulos, Z. Trocsanyi, *$t\bar{t}W^{\pm}$ and $t\bar{t}Z$ hadroproduction at NLO accuracy in QCD with Parton Shower and Hadronization effects*, JHEP **11** (2012) 056, arXiv:1208.2665.

[57] ATLAS Collaboration, *Measurement of the production cross section of jets in association with a Z boson in pp collisions at $\sqrt{s} = 7$ TeV with the ATLAS detector*, submitted to JHEP, arXiv:1304.7098.

[58] ATLAS Collaboration, *Measurement of the cross-section for b-jets produced in association with a Z boson at $\sqrt{s} = 7$ TeV with the ATLAS detector*, Phys. Lett. B **706** (2012) 295, arXiv:1109.1403.

[59] ATLAS Collaboration, *Measurement of the cross-section for W boson production in association with b-jets in pp collisions at $\sqrt{s} = 7$ TeV with the ATLAS detector*, submitted to JHEP, arXiv:1302.2929.

[60] ATLAS Collaboration, *Measurement of the b-tag efficiency in a Sample of Jets Containing Muons with 5 fb^{-1} of data from the ATLAS Detector*, ATLAS-CONF-2012-043, http://cds.cern.ch/record/1435197.

[61] ATLAS Collaboration, *b-jet tagging calibration on c-jets containing D^{*+} mesons*, ATLAS-CONF-2012-039, http://cds.cern.ch/record/1435193.

[62] ATLAS Collaboration, *Measurement of the mistag rate of b-tagging algorithms with 5 fb^{-1} of data collected by the ATLAS detector*, ATLAS-CONF-2012-040, http://cds.cern.ch/record/1435194

[63] T. Junk, *Confidence level computation for combining searches with small statistics*, Nucl. Instr. Meth. **A434** (1999) 435 arXiv:hep-ex/9902006.

[64] A. L. Read, *Presentation of search results: the CLs technique*, J. Phys. G 28 (2002) 2693.

Appendices

A Final $m(Zb)$ distributions separated by lepton final state

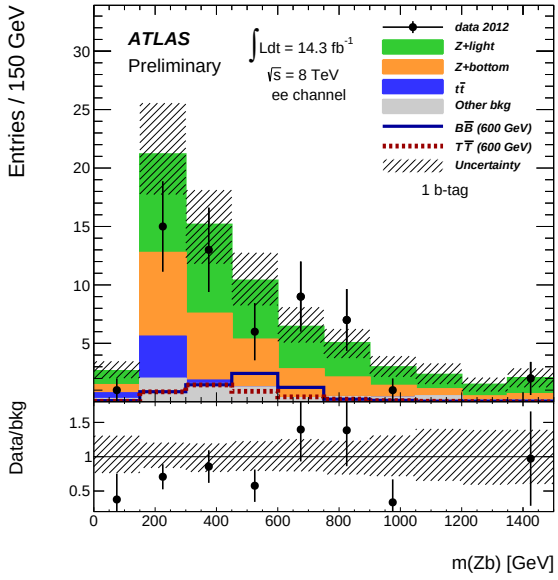

(a)

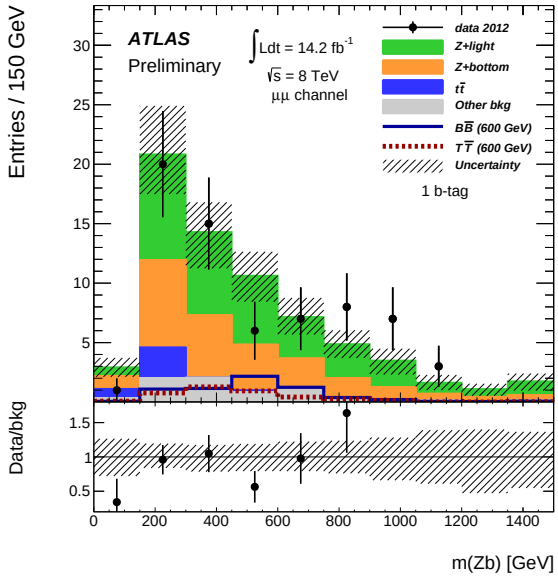

(b)

Figure 12: The $m(Zb)$ distribution after the $p_{\mathrm{T}}(Z)$ and $H_{\mathrm{T}}(\mathrm{jets})$ requirements in (a) $Z \to e^+e^-$ candidate events and (b) $Z \to \mu^+\mu^-$ candidate events containing at least two jets, of which exactly one is b-tagged. The hatched bands in the upper and lower panels represent the total background uncertainty. The rightmost bin in each histogram contains overflow events.

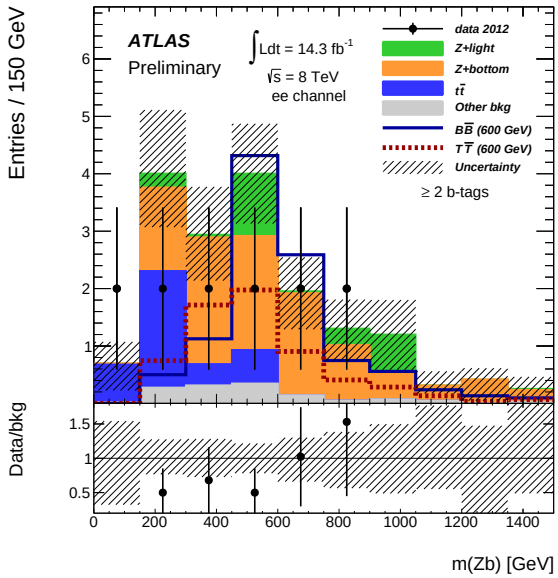

(a)

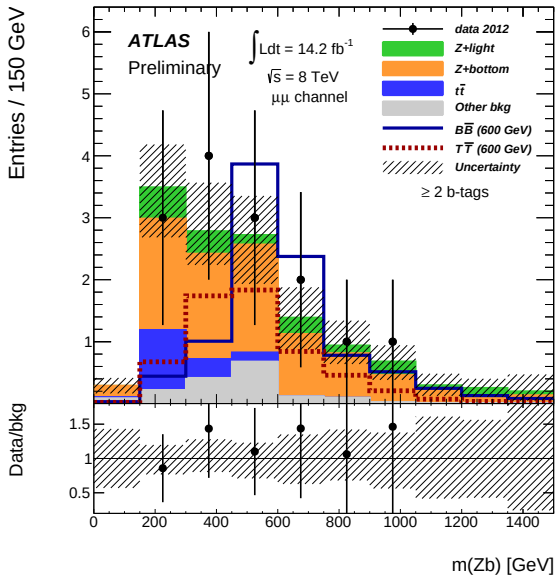

(b)

Figure 13: The $m(Zb)$ distribution after the $p_{\mathrm{T}}(Z)$ and $H_{\mathrm{T}}(\mathrm{jets})$ requirements in (a) $Z \to e^{+}e^{-}$ candidate events and (b) $Z \to \mu^{+}\mu^{-}$ candidate events containing at least two jets, of which at least two are b-tagged. The hatched bands in the upper and lower panels represent the total background uncertainty. The rightmost bin in each histogram contains overflow events.

B Graphical display of events passing the signal sample selection

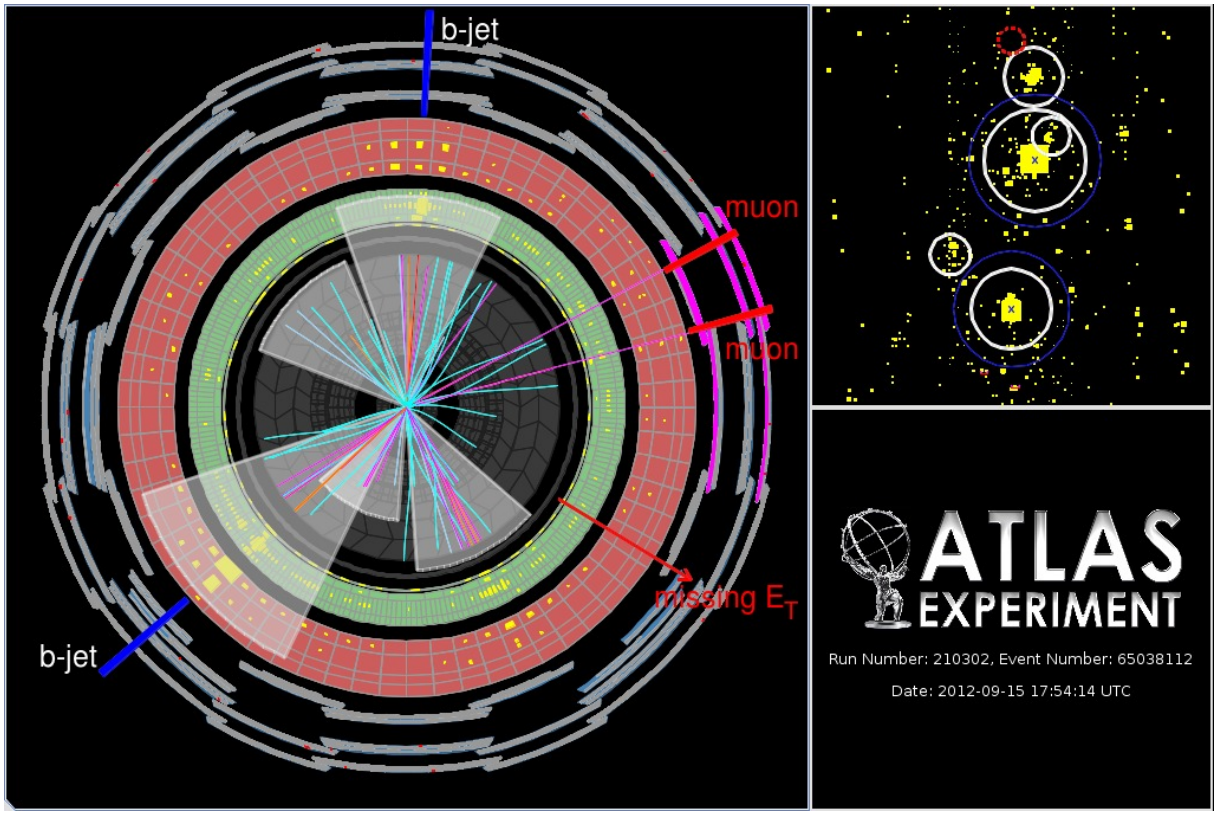

Figure 14: An event in the $\mu\mu$ channel satisfying the final selection criteria. The left panel displays an (x,y) view, while the right panel displays an (η,ϕ) view. The muons are represented in red while the b-tagged jets are represented in blue. The Z candidate is built from the two reconstructed muons and has a p_T of 201 GeV. The Zb system, built with the b-tagged jet with highest p_T, has an invariant mass of 545 GeV. The $H_{\mathrm{T}}(\mathrm{jets})$ variable is 686 GeV.

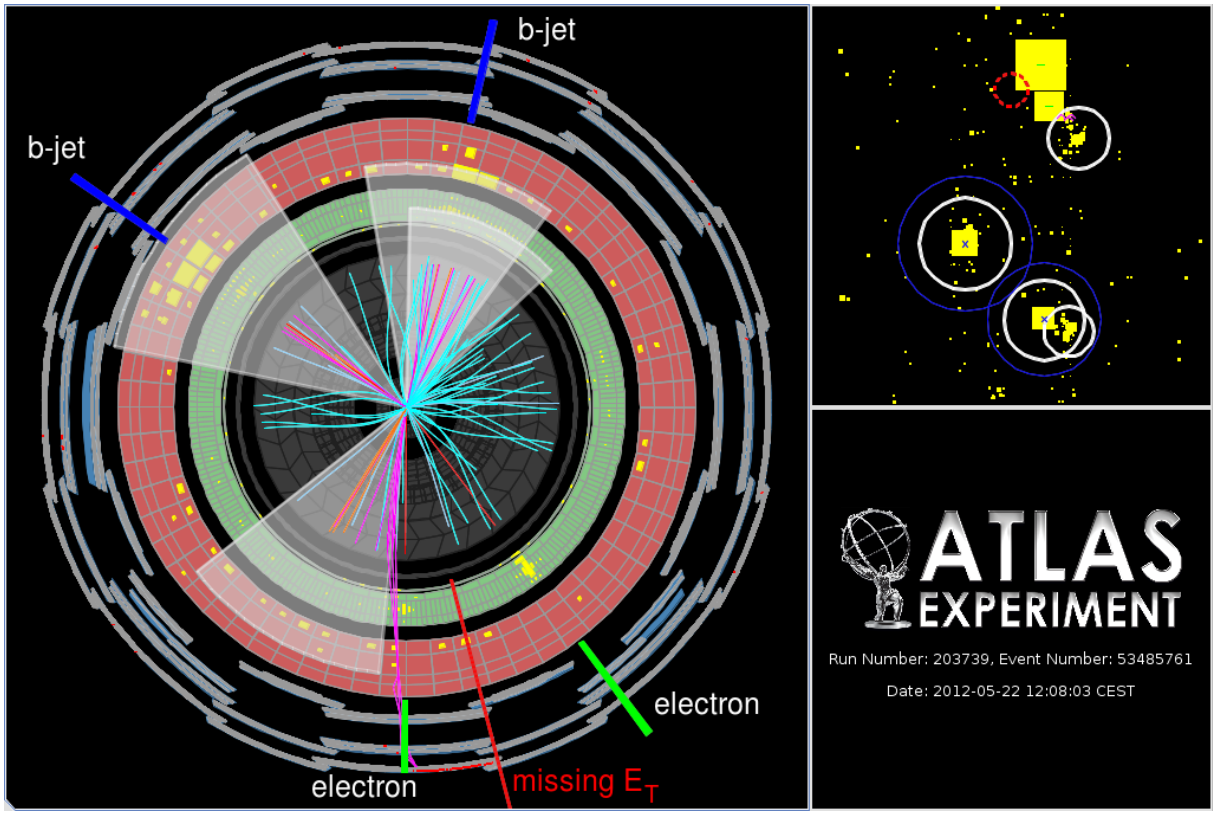

Figure 15: An event in the *ee* channel satisfying the final selection criteria. The left panel displays an (x,y) view, while the right panel displays an (η,ϕ) view. The electrons are represented in green while the *b*-tagged jets are represented in blue. The Z candidate is built from the two reconstructed electrons and has a p_T of 322 GeV. The Zb system, built with the *b*-tagged jet with highest p_T, has an invariant mass of 870 GeV. The $H_{\mathrm{T}}(\mathrm{jets})$ variable is 648 GeV.